The Astronomical Journal, 171:99 (14pp), 2026 February https://doi.org/10.3847/1538-3881/ae246f
© 2026. The Author(s). Published by the American Astronomical Society.
OPEN ACCESS

From Earths to Super-Earths: Five New Small Planets Transiting M Dwarf Stars

Jonathan Gomez Barrientos[1], Heather A. Knutson[1], Morgan Saidel[1,36], Michael Greklek-McKeon[1,2], W. Garrett Levine[3,4], Nicholas Saunders[4,5], Howard Isaacson[6], Renyu Hu[1,7], Karen A. Collins[8], David R. Ciardi[9], Polina A. Budnikova[10], Dmitry V. Cheryasov[10], Samuel W. Yee[8,11], Diogo Souto[12], Aida Behmard[13], Akihiko Fukui[14,15], Avi Shporer[16], Akanksha Khandelwal[17], Bob Massey[18], Brice-Oliver Demory[19,20,21], Catherine A. Clark[9], Chris Stockdale[22], Emily A. Gilbert[9], Enric Palle[15,23], Francis P. Wilkin[24], Felipe Murgas[15,23], Francis Zong Lang[25], Ilse Plauchu-Frayn[26], Jessie L. Christiansen[9], Jon M. Jenkins[27], Joseph D. Twicken[27,28], Keith Horne[29], Michaël Gillon[30], Monika Lendl[31], Michael B. Lund[9], Norio Narita[14,15,32], Pam Rowden[33], Ramotholo Sefako[34], Richard P. Schwarz[8], Steven Giacalone[35], Urs Schroffenegger[25], and Yilen Gómez Maqueo Chew[17]

[1] Division of Geological and Planetary Sciences, California Institute of Technology, Pasadena, CA 91125, USA; jgomezba@caltech.edu
[2] Earth and Planets Laboratory, Carnegie Institution for Science, 5241 Broad Branch Road Northwest, Washington, DC 20015, USA
[3] Department of Earth, Planetary, and Space Sciences, University of California, Los Angeles, CA 90095, USA
[4] Department of Astronomy, Yale University, New Haven, CT 06511, USA
[5] Institute for Astronomy, University of Hawaii at Mānoa, 2680 Woodlawn Drive, Honolulu, HI 96822, USA
[6] 501 Campbell Hall, University of California at Berkeley, Berkeley, CA 94720, USA
[7] Jet Propulsion Laboratory, California Institute of Technology, 4800 Oak Grove Drive, Pasadena, CA 91109, USA
[8] Center for Astrophysics | Harvard & Smithsonian, 60 Garden Street, Cambridge, MA 02138, USA
[9] NASA Exoplanet Science Institute, IPAC, California Institute of Technology, Pasadena, CA 91125, USA
[10] Sternberg Astronomical Institute, M.V. Lomonosov Moscow State University, Universitetskij Prospekt, 13, 119234, Moscow, Russia
[11] Department of Astrophysical Sciences, Princeton University, 4 Ivy Lane, Princeton, NJ 08544, USA
[12] Departamento de Física, Universidade Federal de Sergipe, Avenida Marcelo Deda Chagas, S/N, 49107-230, São Cristóvão, SE, Brazil
[13] Center for Computational Astrophysics, Flatiron Institute, 162 Fifth Avenue, New York, NY 10010, USA
[14] Komaba Institute for Science, The University of Tokyo, 3-8-1 Komaba, Meguro, Tokyo 153-8902, Japan
[15] Instituto de Astrofisica de Canarias, 38205, La Laguna, Tenerife, Spain
[16] Department of Physics and Kavli Institute for Astrophysics and Space Research, Massachusetts Institute of Technology, Cambridge, MA 02139, USA
[17] Universidad Nacional Autónoma de México, Instituto de Astronomía, AP 70-264, Ciudad de México, 04510, Mexico
[18] Villa '39 Observatory, Landers, CA 92285, USA
[19] Center for Space and Habitability, University of Bern, Bern, Switzerland
[20] ARTORG Center for Biomedical Engineering Research, University of Bern, Bern, Switzerland
[21] Space Research and Planetary Sciences, Physics Institute, University of Bern, Bern, Switzerland
[22] Hazelwood Observatory, Australia
[23] Departamento de Astrofísica, Universidad de La Laguna, 38206, La Laguna, Tenerife, Spain
[24] Department of Physics and Astronomy, Union College, 807 Union Street, Schenectady, NY 12308, USA
[25] Center for Space and Habitability, University of Bern, Gesellschaftsstrasse 6, 3012, Bern, Switzerland
[26] Universidad Nacional Autónoma de México, Instituto de Astronomía, AP 106, Ensenada 22860, BC, Mexico
[27] NASA Ames Research Center, Moffett Field, CA 94035, USA
[28] SETI Institute, Mountain View, CA 94043, USA
[29] SUPA Physics and Astronomy, University of St. Andrews, Fife, KY16 9SS Scotland, UK
[30] Astrobiology Research Unit, Université de Liége, Allée du 6 Août 19C, B-4000 Liége, Belgium
[31] Observatoire astronomique de l'Université de Genéve, Chemin Pegasi 51, 1290 Versoix, Switzerland
[32] Astrobiology Center, 2-21-1 Osawa, Mitaka, Tokyo 181-8588, Japan
[33] Royal Astronomical Society, Burlington House, Piccadilly, London W1J 0BQ, UK
[34] South African Astronomical Observatory, P.O. Box 9, Observatory, Cape Town 7935, South Africa
[35] Department of Astronomy, California Institute of Technology, Pasadena, CA 91125, USA
Received 2025 September 11; revised 2025 November 21; accepted 2025 November 24; published 2026 January 19

Abstract

Earth-sized planets transiting M dwarf stars present one of the best opportunities with current facilities for studying the atmospheric and bulk compositions of terrestrial worlds. Here, we statistically validate five new transiting Earth and super-Earth sized planets orbiting M dwarf stars using a combination of light curves from the Transiting Exoplanet Survey Satellite, multicolor observations from Palomar and Las Cumbres Observatory, high-resolution imaging, and stellar spectroscopy. The sample includes TOI-5716 b, an Earth-sized planet ($R_p = 0.96 \pm 0.05\ R_\oplus$) with a 6.766 day orbit around a metal-poor thin-disk star ([Fe/H] $= -0.54 \pm 0.10$); TOI-5728 b, a super-Earth ($R_p = 1.31 \pm 0.05\ R_\oplus$) on an 11.497 day orbit; and TOI-5736 b, a larger planet ($R_p = 1.56 \pm 0.07\ R_\oplus$) with an ultrashort period of just 0.649 days. We also statistically validate a multiplanet system, TOI-5489, hosting two similarly sized super-Earths: TOI-5489 b ($R_p = 1.40 \pm 0.05\ R_\oplus$) and TOI-5489 c ($R_p = 1.28 \pm 0.07\ R_\oplus$) with orbital periods of 3.152 and 4.921 days, respectively. Due to their longer orbital

[36] NSF Graduate Research Fellow.

Original content from this work may be used under the terms of the Creative Commons Attribution 4.0 licence. Any further distribution of this work must maintain attribution to the author(s) and the title of the work, journal citation and DOI.

periods, TOI-5716 b and TOI-5728 b both have equilibrium temperatures $\leqslant 400$ K, making them useful test cases for studies of atmospheric mass loss. If TOI-5728 b is confirmed to have an Earth-like bulk composition, it would join the very small sample of rocky planets orbiting mid-to-late M dwarfs that lie below the cosmic shoreline and therefore may have retained high mean molecular weight atmospheres.

Unified Astronomy Thesaurus concepts: Infrared photometry (792); Transits (1711); Extrasolar rocky planets (511)

1. Introduction

A primary goal of exoplanetary science is to detect and characterize Earth-sized exoplanets, particularly those orbiting within or near the habitable zones of their host stars. While detecting and characterizing these worlds around Sun-like stars presents significant challenges, some of these challenges can be mitigated by concentrating on transiting Earth-sized planets that orbit M-type stars—the most abundant stellar type in the Milky Way (T. J. Henry et al. 1994; J. D. Kirkpatrick et al. 1999). The smaller radii of M dwarfs result in deeper and more frequent planetary transits compared to similar planets orbiting Sun-like stars, making them more favorable targets for atmospheric characterization via transmission spectroscopy. The lower masses of M dwarfs also result in larger radial velocity semiamplitudes, making planets around these stars more favorable targets for radial velocity mass measurements. For these reasons, small planets around M dwarfs offer an unprecedented opportunity to characterize the bulk densities and atmospheric or surface properties of terrestrial worlds using current ground-based and space-based telescopes (e.g., P. Nutzman & D. Charbonneau 2008; R. Wordsworth & L. Kreidberg 2022).

However, despite these observational advantages, M dwarfs also present unique challenges for atmospheric characterization studies. Although it is easier to detect atmospheric signals from Earth-sized planets transiting M dwarfs, they may be less likely to retain their primary atmospheres than their counterparts around Sun-like stars (Y. Hori & M. Ogihara 2020). M dwarfs emit more frequent flares and have higher fractional X-ray and extreme-ultraviolet (XUV) fluxes, which can more efficiently strip away the gaseous envelopes of planets with equivalent equilibrium temperatures (R. M. Roettenbacher & S. R. Kane 2017; D. P. Fleming et al. 2020). There is abundant observational evidence indicating that most small planets on close-in orbits around M dwarfs lack thick atmospheres (e.g., T. P. Greene et al. 2023; S. Zieba et al. 2023; Q. Xue et al. 2024; M. Zhang et al. 2024; M. Fortune et al. 2025; L. Kreidberg & K. B. Stevenson 2025; R. Luque et al. 2025; E. A. Meier Valdés et al. 2025; P. Wachiraphan et al. 2025), but current surveys have not yet been able to determine the minimum orbital separation outside which rocky planets consistently retain high mean molecular weight atmospheres.

The concept of the "cosmic shoreline" was first introduced by K. J. Zahnle & D. C. Catling (2017), who observed that in the solar system it is possible to draw a line in total insolation versus escape velocity that separates rocky bodies with and without atmospheres. While it is the XUV irradiation that drives atmospheric mass loss, this study pointed out that total insolation can be converted to an equivalent XUV irradiation for FGK and early M stars using a simple power-law scaling. More recently, E. K. Pass et al. (2025) extended this framework to mid-to-late M stars, which exhibit unique activity histories compared to early M stars and FGK stars and therefore require a different approach to estimate their time-integrated XUV fluxes.

Our ability to observationally test the cosmic shoreline framework for both early and mid-to-late M dwarfs is currently limited by the small number of confirmed rocky planets with low equilibrium temperatures transiting nearby M dwarfs. To this end, we statistically validate the planetary nature of five small ($<1.8\ R_\oplus$) Transiting Exoplanet Survey Satellite (TESS) planet candidates transiting early to mid M dwarfs ($T_{\rm eff}$ of 3300−3900 K): TOI-5489.01, TOI-5489.02, TOI-5716.01, TOI-5728.01, and TOI-5736.01. Four of these candidates have predicted equilibrium temperatures lower than 650 K, and two are $\leqslant$400 K, making them useful for constraining the location of the cosmic shoreline. We begin by describing the observations of our targets in Section 2, including the TESS photometry, multicolor ground-based photometry, high-resolution imaging, and stellar spectroscopy. Our light-curve modeling procedure is described in Section 3 and our statistical validation analysis in detailed in Section 4. We present our results in Section 5 and discuss their implications in Section 6. Finally, we summarize our conclusions in Section 7.

2. Observations

In this section, we detail the collection and reduction of the space-based and ground-based observations of our targets.

2.1. TESS Photometry

All of our targets (see Table 1) were initially identified by TESS through the detection of their periodic transit signals. In this work, we utilized all available 2 minute cadence presearch data conditioning simple aperture photometry (J. C. Smith et al. 2012; M. C. Stumpe et al. 2012; M. C. Stumpe et al. 2014) light curves from the TESS Science Processing Operations Center Transiting Planet Search (SPOC TPS) pipeline (J. M. Jenkins et al. 2016). We accessed the publicly available photometry for our five TESS candidates (TOI-5489.01, TOI-5489.02, TOI-5716.01, TOI-5728.01, and TOI-5736.01) through the Mikulski Archive for Space Telescope using the Python package `lightkurve` (Lightkurve Collaboration et al. 2018). Prior to their release as TESS object of interest (TOI) alerts, all candidates had been vetted by the TESS Science Office using automated search pipelines (N. M. Guerrero et al. 2021).

To ensure optimal photometric quality for subsequent transit analysis, we performed additional processing on the retrieved TESS observations. We first masked the transit signals and applied a Lomb–Scargle periodogram (N. R. Lomb 1976; J. D. Scargle 1982) to identify any residual periodic trends that might impact the quality of individual transits. This analysis revealed systematic trends in all five targets' TESS light curves, with periods ranging from 4.8 to 9.6 days (TOI-5489: 8.4 days; TOI-5716: 9.6 days; TOI-5728: 4.8 days; and

Table 1
Summary of Stellar Properties

Parameter	TOI-5489[a]	TOI-5716[b]	TOI-5728[c]	TOI-5736[a]
TIC ID	468983280	298074836	219875976	310380289
R.A.	08:34:45.91	13:27:36.19	17:21:24.22	14:15:02.02
Decl.	+11:29:22.52	+73:10:38.76	+67:33:01.52	+49:30:03.38
TESS (mag)	11.69	13.10	12.49	11.98
V (mag)	13.82	15.83	15.02	13.55
J (mag)	10.28	11.57	11.00	10.83
$T_{\rm eff}$ (K)	3547 ± 157	3436 ± 79	3419 ± 70	3949 ± 157
[Fe/H]	⋯	−0.54 ± 0.10	−0.12 ± 0.09	⋯
R_* ($R_\odot$)	0.42 ± 0.01	0.22 ± 0.01	0.37 ± 0.01	0.58 ± 0.02
M_* ($M_\odot$)	0.41 ± 0.02	0.19 ± 0.01	0.36 ± 0.02	0.57 ± 0.02
Parallax (mas)	22.36 ± 0.02	25.41 ± 0.02	18.23 ± 0.02	10.82 ± 0.01
RV (km s^{-1})	37.71 ± 0.89[d]	25.50 ± 0.10[e]	−6.81 ± 0.10[e]	−1.76 ± 0.99[d]

Notes.
[a] Stellar properties originate from the TESS Input Catalog (TIC; K. G. Stassun et al. 2019).
[b] $T_{\rm eff}$, and [Fe/H] were derived from APOGEE spectra as described in Section 2.4.2. R_* and M_* were derived using `isoclassify`. All other values are from the TIC.
[c] $T_{\rm eff}$, and [Fe/H] were derived from High Resolution Echelle Spectrometer (HIRES) spectra using the SpecMatch-Emp tool (S. W. Yee et al. 2017) as described in Section 2.4. R_* and M_* were derived using `isoclassify`. All other values are from the TIC.
[d] From Gaia Data Release 3 (e.g., D. Katz et al. 2023).
[e] From Keck/HIRES.

TOI-5736: 6.5 days). To address these systematic effects, we modeled the residual periodicity using a Gaussian kernel convolution following the methodology described in M. Greklek-McKeon et al. (2023), then divided out these trends to produce flattened TESS light curves.

2.2. Multicolor Transit Photometry

Here, we present the multicolor transit observations of our targets.

2.2.1. Palomar Photometry

We obtained J-band transit observations of four TESS candidates (TOI-5489.02, TOI-5716.01, TOI-5728.01, and TOI-5736.01) using the Wide-field Infrared Camera (J. C. Wilson et al. 2003) on the 200 inch Hale Telescope at Palomar Observatory. These targets were observed through a combination of dedicated telescope time and downtime allocated to other programs. All observations employed a beam-shaping diffuser that produces a top-hat point-spread function (PSF) with an FWHM of 3″. This diffuser provided two key advantages: it stabilized the PSFs to reduce correlated noise from changing atmospheric conditions (G. Stefansson et al. 2017; S. Vissapragada et al. 2020), and it increased observing efficiency by enabling longer exposure times for bright targets. In Table 2 we provide a summary of the observations.

Next, we extracted light curves for each target using the same general approach as in previous studies (S. Vissapragada et al. 2020; M. Greklek-McKeon et al. 2023). We first flat-fielded, dark subtracted, and corrected the images for hot and dead pixels following the procedures detailed in S. Vissapragada et al. (2020). We then performed circular aperture photometry using the Python package `photutils` on all stars identified by the DAOStarFinder algorithm (P. B. Stetson 1987). This algorithm detects stars that meet or exceed a manually specified signal-to-noise ratio threshold, which we set between 100 and 400 depending on the target brightness and field star density.

To optimize the photometric precision, we tested aperture radii ranging from 5 to 30 pixels in steps of 1 pixel for each target. For each aperture size, we extracted light curves for both the target and up to 10 comparison stars, then detrended the target light curve by dividing it by the mean light curve of all comparison stars. We calculated the rms of the detrended data and selected the aperture size that minimized the target's light-curve rms for all subsequent analyses.

2.2.2. LCOGT Photometry

We obtained multicolor transit observations of three TESS candidates (TOI-5489.01, TOI-5489.02, and TOI-5736.01) with nodes from the Las Cumbres Observatory global telescope (LCOGT) network (T. M. Brown et al. 2013), including the 1 m facilities at Teide Observatory, Tenerife (Teide), McDonald Observatory, Fort Davis, Texas (McD), Siding Spring Observatory, Australia (SSO), Cerro Tololo Inter-American Observatory, Chile (CTIO), and South African Astronomical Observatory, South Africa (SAAO), plus the 2 m facility at Faulkes Telescope North (FTN), Haleakala Observatory, Maui, Hawai'i. Each 1 m telescope houses a 4096 × 4096 SINISTRO camera with 0.″389 pixel^{-1} resolution, providing a 26′ × 26′ field of view. The 2 m telescope employs the MuSCAT3 multiband imager (N. Narita et al. 2020). We processed all LCOGT data using the standard `BANZAI` calibration pipeline (C. McCully et al. 2018) and performed differential photometry using `AstroImageJ` (K. A. Collins et al. 2017). Details of the observations are provided in Table 2.

2.2.3. SAINT-EX Photometry

We obtained $I+z$–band transit observations of TOI-5716.01 using the 1.0 m Search and Characterisation of Transiting Exoplanets (SAINT-EX) telescope (B. O. Demory et al. 2020; Y. Gómez Maqueo Chew et al. 2023), located at the Sierra de San Pedro Mártir Observatory in Baja California,

Table 2
Ground-based Light-curve Observation Details

TOI	Observatory	r_{phot}[a] (arcsec)	Date (UTC)	Start Time	End Time	Filter (s)	t_{exp} (s)	Airmass Start/Middle/End	σ/σ_{phot}[c]
5489.01	LCOGT-McD	5.06	2022-12-11	05:47:19	08:53:25	i'	37	2.27/1.39/1.12	1.2
5489.01	LCOGT-McD	7.39	2023-02-09	03:03:03	06:23:41	i'	37	1.51/1.14/1.06	1.1
5489.01	LCOGT-CTIO	5.84	2023-02-09	03:02:54	06:23:56	i'	37	1.39/1.36/1.68	1.5
5489.01	LCOGT-SSO	5.45	2023-02-15	10:21:09	13:42:25	i'	37	1.84/1.41/1.39	1.4
5489.01	LCOGT-SAAO	5.45	2023-02-21	18:25:55	21:02:32	i'	37	1.90/1.50/1.39	2.0
5489.01	LCOGT-Teid	4.67	2024-01-02	22:56:18	02:19:42	i'	37	1.87/1.22/1.06	1.4
5489.02	LCOGT-SAAO	3.89	2025-01-01	20:50:15	00:33:34	i'	37	2.70/1.54/1.39	2.6
5489.02	LCOGT-McD	3.89	2025-02-04	07:34:11	11:04:42	i'	37	1.09/1.35/2.38	1.5
5489.02	LCOGT-CTIO	6.61	2025-04-28	23:35:20	02:41:33	i'	37	1.37/1.66/2.82	1.4
5489.02	Palomar-Hale	3.75	2024-12-07	07:14:35	09:56:44	J	28	2.02/1.39/1.15	4.9
5716.01	Palomar-Hale	4.00	2025-01-24	08:57:07	14:20:58	J	36	1.55/1.32/1.32	3.3
5716.01	SAINT-EX	4.20	2025-01-24	09:24:29	14:00:18	$I+z$	46	1.54/1.38/1.36	1.0
5716.01	SAINT-EX	4.55	2025-04-22	07:01:17	12:28:54	$I+z$	50	1.34/1.52/1.86	1.0
5728.01	Palomar-Hale	4.00	2024-10-10	02:26:09	06:20:00	J	40	1.32/1.59/2.13	3.5
5736.01	Palomar-Hale	3.50	2024-07-28	03:50:32	07:07:32	J	30	1.15/1.42/2.06	3.8
5736.01	LCOGT-FTN	7.56	2024-02-19	10:34:07	16:01:09	g', r', i', z_s	60/23/23/27	1.82/1.20/1.18	1.2/1.4/1.5/1.6
5736.01[b]	LCOGT-FTN	5.67	2024-03-27	10:42:15	15:30:03	g', r', i', z_s	60/23/23/27	1.21/1.15/1.47	1.1/1.4/1.4/1.6
5736.01	LCOGT-FTN	7.83	2025-01-02	12:53:12	15:47:25	g', r', i', z_s	60/23/23/27	2.32/1.57/1.26	1.4/2.0/1.9/2.1
5736.01	LCOGT-FTN	7.29	2025-05-14	05:51:54	09:01:41	g', r', i', z_s	60/23/23/27	1.52/1.24/1.14	1.1/1.4/1.5/1.6
5736.01	LCOGT-Teid	5.06	2024-03-04	01:36:54	06:28:57	i'	42	1.30/1.08/1.16	1.0
5736.01	LCOGT-McD	4.28	2024-04-02	06:52:13	11:46:23	i'	42	1.11/1.07/1.34	1.5

Notes.
[a] Radius of optimal photometric aperture.
[b] The observations in r', i', and z_s exhibit correlated noise and were excluded from the global fit.
[c] The true uncertainty in the data divided by the photon noise.

México. SAINT-EX is a Ritchey-Chrétien $f/8$ telescope equipped with a thermoelectrically cooled 2048 × 2048 Andor iKon-L CCD camera, providing a pixel scale of $0\farcs35$ and a field of view of $12' \times 12'$. Observations were conducted on 2025 January 24 and 2025 April 22 (UT). We reduced and analyzed the photometric data using `AstroImageJ` (K. A. Collins et al. 2017). A summary of the observations is provided in Table 2.

2.3. High Angular Resolution Imaging

We downloaded all available high-resolution images and corresponding contrast curves for each target from the ExoFOP website[37] to check for unresolved stellar companions that may potentially dilute or host the observed transit signals. These observations revealed no nearby stellar companions for any of our five targets (see Figure 1). For targets with multiple contrast curves, we selected the observation with the best contrast sensitivity (see Table 3) for our subsequent statistical validation analysis with `TRICERATOPS+` (J. Gomez Barrientos et al. 2025).

2.3.1. SAI-2.5 m

TOI-5716 was observed on 2023 October 16 UT, with the speckle polarimeter on the 2.5 m telescope at the Caucasian Observatory of Sternberg Astronomical Institute (SAI-2.5 m) of Lomonosov Moscow State University. A low-noise CMOS detector Hamamatsu ORCA-quest was used as a detector. The atmospheric dispersion compensator was active, which allowed the use of the I_c band. The respective angular resolution is $0\farcs083$. 2500 frames each with an exposure of 60 ms were accumulated. No companion was detected. We calculated the standard deviation in concentric ring zones within the autocorrelation function (see inset in the upper right panel of Figure 1). This standard deviation multiplied by a factor of 5 was converted to the expected magnitude difference between the host star and a possible stellar companion (I. A. Strakhov et al. 2023). The detection limits at distances of $0\farcs25$ and $1\farcs0$ from the star are $\Delta I_c = 3.8$mag and 4.5 mag, respectively.

2.3.2. Palomar and Keck2/NIRC2

TOI-5489 was observed on 2023 November 29 UT with the PHARO instrument (T. L. Hayward et al. 2001) on the Palomar-Hale (5 m) behind the P3K natural guide star adaptive optics (AO) system (R. Dekany et al. 2013). The pixel scale for PHARO is $0\farcs025$. The Palomar data were collected in a standard five-point quincunx dither pattern. Observations of TOI-5728 and TOI-5736 were made on 2023 June 10 UT with the NIRC2 instrument on Keck II (10 m) behind the natural guide star AO system (P. Wizinowich et al. 2000) in the standard three-point dither pattern that is used with NIRC2 to avoid the left lower quadrant of the detector. All observations were made in the K_{cont} filter. Flat fields were taken on sky, dark subtracted, and median averaged, and sky frames were generated from the median average of the dithered science frames. Each science image was then sky subtracted and flat-fielded. The reduced science frames were combined into a single mosaiced image with final resolutions of $\sim0\farcs11$, $\sim0\farcs056$, and $\sim0\farcs056$, respectively. The sensitivity of the final combined AO images were determined by injecting simulated

[37] https://exofop.ipac.caltech.edu/tess/.

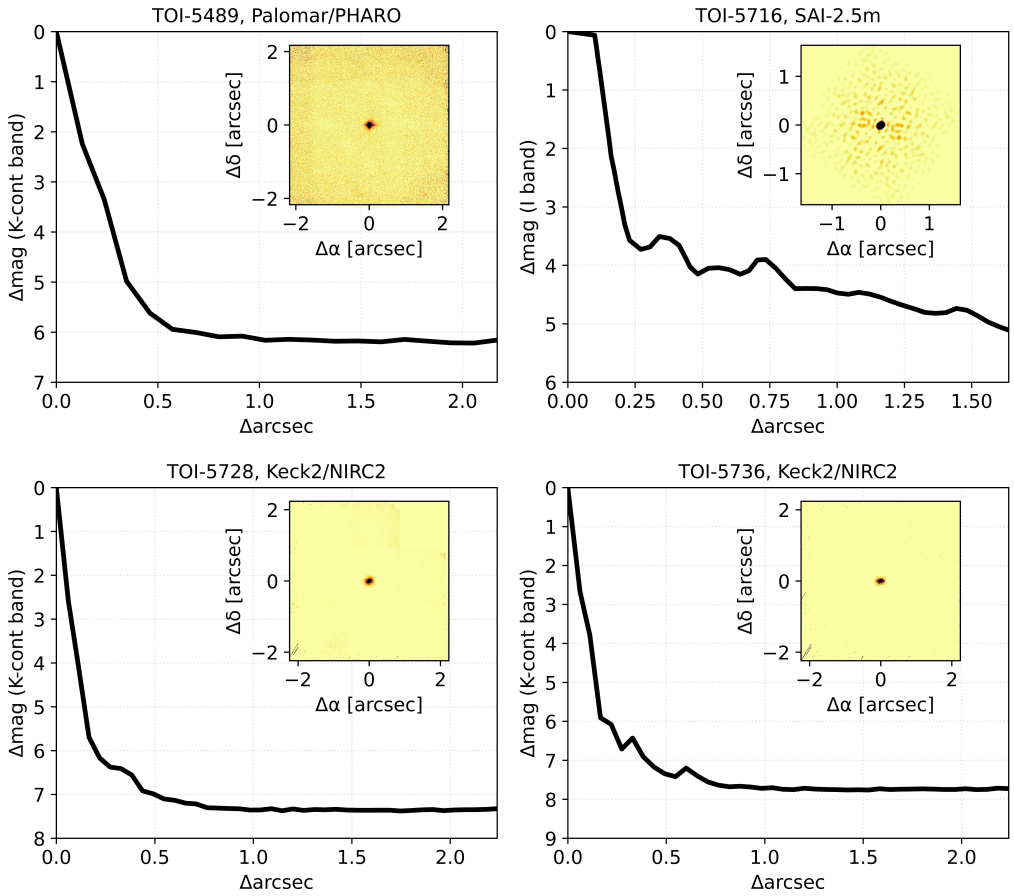


Figure 1. High-resolution images and corresponding contrast curves (black line) of our targets. There are no secondary sources detected around any of the targets.

sources azimuthally around the primary target every 20° at separations of integer multiples of the central source's FWHM (E. Furlan et al. 2017). The brightness of each injected source was scaled until standard aperture photometry detected it with 5σ significance. The final 5σ limit at each separation was determined from the average of all of the determined limits at that separation and the uncertainty on the limit was set by the rms dispersion of the azimuthal slices at a given radial distance. No stellar companions were detected.

2.4. High-resolution Spectroscopy

In this section, we proceed to describe our spectroscopic observations of the host stars of our targets.

2.4.1. HIRES Spectra

We obtained observations of TOI-5716 and TOI-5728 with HIRES (S. S. Vogt et al. 1994) on the Keck I Telescope. For each target, we collected one out-of-transit, iodine-free spectrum on 2025 June 8 UT adopting an exposure time of 1800 s for TOI-5716 and 1200 s for TOI-5728. We provide the measured radial velocities in Table 1. To empirically derive spectroscopic stellar parameters, we used the SpecMatch-Emp routine (S. W. Yee et al. 2017), which crossmatches a given HIRES spectrum with a library of high signal-to-noise ratio observed spectra of stars with empirically determined stellar parameters. The technique is especially effective for late-type stars for which synthetic spectra are limited due to incomplete line lists.

For TOI-5728 we find $[\mathrm{Fe/H}] = -0.12 \pm 0.09$ and $T_{\mathrm{eff}} = 3419 \pm 70$ K, which is in agreement with the TIC (K. G. Stassun et al. 2019) value of $T_{\mathrm{eff}} = 3444 \pm 157$ K. For TOI-5716 we find $[\mathrm{Fe/H}] = -0.45 \pm 0.09$ and $T_{\mathrm{eff}} = 3269 \pm 70$ K, which is also in agreement with the TIC value of $T_{\mathrm{eff}} = 3331 \pm 157$ K. We note that $[\mathrm{Fe/H}] = -0.45$ lies at the lower boundary of the spectral library used by SpecMatch-Emp, and conclude that the true metallicity of TOI-5716 may be lower than this value.

For TOI-5728, we derive R_* and M_* with the Python package `isoclassify` (D. Huber et al. 2017; T. A. Berger et al. 2020, 2023). The package incorporates spectroscopic information (e.g., T_{eff} and [Fe/H]), photometry (e.g., K magnitude), and Gaia parallax to derive stellar parameters. In our calculation, we selected the MESA Isochrones and Stellar Tracks (J. Choi et al. 2016) and adopted the default settings. The derived values are given in Table 1. We note that these values are consistent with the TIC values of $R_* = 0.376 \pm 0.011$ $R_\odot$ and $M_* = 0.364 \pm 0.020$ $M_\odot$, which are calculated using the K_S-band magnitude relations from A. W. Mann et al. (2015) and A. W. Mann et al. (2019).

2.4.2. APOGEE Spectra

We analyzed the H-band (1.51–1.60 μm) APOGEE high-resolution ($R \sim 22{,}500$; R. F. Wilson et al. 2018) spectra of TOI-5716 to determine precise stellar parameters and individual abundances. APOGEE is a cryogenic multifiber spectrograph located in both hemispheres (J. A. Kollmeier et al. 2026) with

Table 3
Details of the High-resolution Imaging

TOI	Telescope	Instrument	Filter	Image Type
5489				
	WIYN (3.5 m)	NESSI	832 (40) nm	Speckle
	WIYN (3.5 m)	NESSI	562 (44) nm	Speckle
	SAI-2.5 m (2.5 m)	Speckle Polarimeter	I	Speckle
	Palomar (5 m)	PHARO	K_{cont}	AO
	SOAR (4.1 m)	HRCam	I	Speckle
5716				
	SAI-2.5 m (2.5 m)	Speckle Polarimeter	I	Speckle
5728				
	WIYN (3.5 m)	NESSI	562 (44) nm	Speckle
	Keck2 (10 m)	NIRC2	K_{cont}	AO
	SAI-2.5 m (2.5 m)	Speckle Polarimeter	I	Speckle
	WIYN (3.5 m)	NESSI	832 (40) nm	Speckle
5736				
	Gemini (8 m)	Alopeke	832 (40) nm	Speckle
	Gemini (8 m)	Alopeke	562 (54) nm	Speckle
	WIYN (3.5 m)	NESSI	832 (40) nm	Speckle
	WIYN (3.5 m)	NESSI	562 (44) nm	Speckle
	Keck2 (10 m)	NIRC2	K_{cont}	AO
	SAI-2.5 m (2.5 m)	Speckle Polarimeter	I	Speckle

Note. The observations adopted in our statistical validation analysis are marked in bold.

ongoing observations for the Milky Way Mapper project within the fifth-generation Sloan Digital Sky Survey. We used the normalized public APOGEE DR19 spectra (D. L. Nidever et al. 2015; S. Collaboration et al. 2025) in this study.

Previous studies have utilized APOGEE data to measure the metallicity of TOI-5716, though with varying results and limitations. TOI-5716 is included in the APOGEE DR16 catalog (R. Ahumada et al. 2020), with a reported metallicity of $[m/H] = -1$. However, J. Birky et al. (2020) and D. Souto et al. (2021) both found that this catalog is biased toward reporting higher temperatures and lower metallicities for M dwarfs. J. Birky et al. (2020) instead derive their own catalog using The Cannon, a machine learning algorithm for spectral classification (M. Ness et al. 2015; A. R. Casey et al. 2016), and

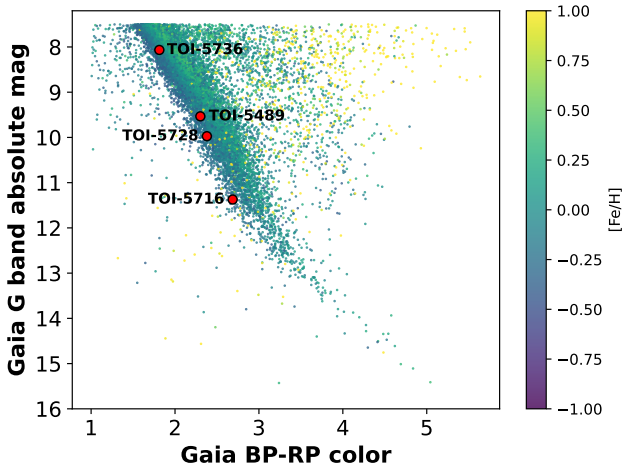


Figure 2. Gaia color–magnitude diagram of our targets, along with the catalog of M stars from J. Birky et al. (2020). The data points are color coded by their metallicity from J. Birky et al. (2020). The location of TOI-5716 is consistent with the most metal-poor subset of this population, in good agreement with our spectroscopic analysis.

report $[m/H] = -0.77 \pm 0.08$ for TOI-5716. However, as shown in Figure 2 of J. Birky et al. (2020), this metallicity lies outside the range of their training data, which only extends to $[m/H] = -0.5$, and therefore may also suffer from edge effects.

Given the limitations surrounding SpecMatch-Emp and previous work in deriving reliable spectroscopic parameters for TOI-5716, we performed a detailed analysis based on the high-resolution near-infrared (NIR) spectra from APOGEE. M dwarf atmospheric parameters and elemental abundances are more effectively constrained in the NIR, where these stars are significantly brighter and exhibit fewer and less complex molecular features compared to the optical regime (F. Allard et al. 2000). We adopted the methodology described in D. Souto et al. (2020) to derive the stellar atmospheric parameters (T_{eff} and $\log g$) and individual abundances of C, O, Mg, Al, K, Ca, and Ti (see E. Melo et al. 2024). Using this framework, we derived values of $T_{eff} = 3436 \pm 79$ K and $\log g = 4.9 \pm 0.13$ dex for TOI-5716. This effective temperature is slightly higher than the one derived using HIRES (3269 ± 70 K), but still consistent at the 1.6σ level. We obtain $[Fe/H] = -0.54 \pm 0.10$ dex from our fit to the APOGEE spectra, in good agreement with the $[Fe/H] = -0.45 \pm 0.09$ value estimated using HIRES spectra. We further verify this result by plotting TOI-5716, along with our other targets, in a color–magnitude diagram. As shown in Figure 2, TOI-5716 lies below the solar-metallicity locus. Lastly, using the APOGEE spectra, we also constrain the elemental abundances of the following species: $[C/Fe] = 0.07 \pm 0.04$, $[O/Fe] = 0.13 \pm 0.04$, $[Mg/Fe] = -0.04 \pm 0.13$, $[Al/Fe] = -0.24 \pm 0.11$, $[K/Fe] = 0.07 \pm 0.08$, $[Ca/Fe] = 0.13 \pm 0.08$, and $[Ti/Fe] = -0.13 \pm 0.10$. Having obtained reliable spectroscopic parameters for TOI-5716, we followed the same approach as with TOI-5728 to derive R_* and M_* and report our results in Table 1. Similar to TOI-5728, our derived values are consistent with the TIC values of $R_* = 0.226 \pm 0.007$ $R_\odot$ and $M_* = 0.195 \pm 0.020$ $M_\odot$.

3. Light-curve Modeling

We used our photometric transit data to characterize the properties of each TESS candidate and investigate potential wavelength-dependent transit depth variations. To do so, we first

Table 4
Posterior Results From the Joint Fit of the TESS and Ground-based Light Curves

TOI	$t_0 - 2457000$[a] (BTJD)	P[b] (days)	a/R_*	b	i (deg)	R_p/R_*[c]	R_p ($R_\oplus$)	T_{eq}[d] (K)
5489 b	$1493.70710^{+0.00110}_{-0.00115}$	$3.15222^{+0.00001}_{-0.00001}$	$16.26^{+0.48}_{-0.48}$	$0.391^{+0.083}_{-0.133}$	88.6 ± 0.50	$0.0308^{+0.0010}_{-0.0010}$	$1.40^{+0.05}_{-0.05}$	624
5489 c	$1496.32542^{+0.00215}_{-0.00210}$	$4.92126^{+0.00001}_{-0.00001}$	$21.83^{+0.66}_{-0.66}$	$0.449^{+0.080}_{-0.138}$	88.8 ± 0.40	$0.0281^{+0.0014}_{-0.0014}$	$1.28^{+0.07}_{-0.07}$	536
5716 b	$1683.61514^{+0.00164}_{-0.00161}$	$6.76630^{+0.00001}_{-0.00001}$	$39.00^{+1.17}_{-1.21}$	$0.410^{+0.075}_{-0.102}$	89.40 ± 0.15	$0.0390^{+0.0014}_{-0.0014}$	$0.96^{+0.05}_{-0.05}$	400
5728 b	$1685.08679^{+0.00120}_{-0.00118}$	$11.49761^{+0.00003}_{-0.00003}$	$39.90^{+0.78}_{-0.98}$	$0.117^{+0.107}_{-0.083}$	89.83 ± 0.15	$0.0319^{+0.0009}_{-0.0009}$	$1.31^{+0.05}_{-0.05}$	382
5736 b	$1738.89683^{+0.00155}_{-0.00143}$	$0.64899^{+0.00001}_{-0.00001}$	$4.53^{+0.13}_{-0.13}$	$0.435^{+0.145}_{-0.242}$	84.5 ± 2.2	$0.0247^{+0.0007}_{-0.0007}$	$1.56^{+0.07}_{-0.07}$	1311

Notes.
[a] Transit midtime of the first transit in the TESS time series.
[b] Derived from a separate transit fit to the TESS data.
[c] Weighted average of R_p/R_* values from TESS and ground-based data.
[d] The planet's equilibrium temperature assuming full day–night heat redistribution and zero albedo.

fit the individual TESS transits, then phase folded the TESS data on the best-fit period, and finally performed a joint fit of the phase-folded TESS data with the ground-based light curves.

We modeled the light curves of our targets using the `exoplanet` package, which couples the forward light-curve model `starry` (R. Luger et al. 2019) with `PyMC3's` No U-turn Sampler (M. D. Hoffman & A. Gelman 2011) to explore the parameter space. In all fits, we simultaneously modeled both the transit signal and systematic effects in the ground-based light curves. For the transit model, we assumed circular orbits (i.e., zero orbital eccentricity) for all planets. We tested the validity of this assumption for TOI-5716 b and TOI-5728 b, which have the longest orbital periods in our sample, by repeating our fits with $e\cos\omega$ and $e\sin\omega$ as free parameters and placing a prior on the eccentricity e following D. M. Kipping (2013). We found that the retrieved posteriors for e are consistent with circular orbits for both planets, and that the data provide relatively weak constraints on this parameter. We therefore fixed $e = 0$ in our final version of the fits for all five planets. We also adopted a quadratic limb darkening law with fixed coefficients calculated using `ExoTIC-LD` (D. Grant & H. R. Wakeford 2022) for each bandpass, based on the stellar properties reported in Table 1. We also explored fits where we allowed the limb darkening coefficients to vary as free parameters with either broad uniform priors or normal priors centered on the predicted values with widths calculated by propagating the uncertainties in the stellar parameters. We found that this yielded equivalent R_p/R_* posteriors, indicating that the precision of our light curves is not high enough for us to be sensitive to these effects.

The transit model included four global parameters: the semimajor axis in stellar radius units (a/R_*), the impact parameter (b), the transit epoch (t_0), and the orbital period (P). For joint fits of phase-folded TESS data and ground-based light curves, we treated P as a free parameter with a Gaussian prior centered on the TESS-only fit value and bounded by its uncertainties. We also fit for separate planet-to-star radius ratios (R_p/R_*) in each bandpass to search for potential wavelength-dependent depth variations. For the TESS data, we included a parameter (k) that scaled the reported TESS error bars to match the observed scatter in the residuals (i.e., $\sigma = \sigma_{\rm orig} \cdot k$). Similarly, for the ground-based data we fit a jitter term that is added in quadrature to the Poisson noise ($\sigma^2 = \sigma^2_{\rm Poisson} + \sigma^2_{\rm systematic}$).

Our systematics model was designed to capture variations in all the ground-based light curves due to changing atmospheric conditions and instrumental effects. This model incorporated weighted contributions from comparison starlight curves, with the weights treated as free parameters. We also included weights for the airmass, PSF width, sky background flux, and distances from the median centroid position as candidate covariates. To optimize the systematics model for each ground-based light curve, we selected the combination of detrending parameters that minimized the Bayesian information criterion (G. Schwarz 1978) prior to performing the joint fit with the phase-folded TESS data. In Table 4, we provide the results of our fits.

4. Statistical Validation

For each TESS candidate, we calculated the probability that it might be an astrophysical false positive using `TRICERATOPS+`[38] (J. Gomez Barrientos et al. 2025), a modified version of `TRICERATOPS` (S. Giacalone et al. 2021). This Python package employs a Bayesian framework that combines information about the transit shape measured by TESS and (when available) AO imaging data with prior knowledge of stellar populations in the Milky Way to calculate both the false-positive probability (FPP) and nearby FPP (NFPP) for each planet candidate. The FPP quantifies the likelihood that a transit signal does not originate from a planet transiting the target star, while the NFPP represents the probability that the observed transit signal stems from a resolved nearby star. In J. Gomez Barrientos et al. (2025), we updated this framework to incorporate information from multicolor ground-based transit photometry, which has a higher angular resolution than TESS and can significantly reduce both the FPP and the NFPP. Following S. Giacalone et al. (2021), we require planet candidates to satisfy $\mathrm{FPP} < 0.015$ and $\mathrm{NFPP} < 10^{-3}$ to be considered statistically validated planets. We note that for most of our targets, the FPP values are orders of magnitude below these thresholds. Among our five targets, TOI-5716 b has the highest FPP at 4.3×10^{-3}. As recommended by S. Giacalone et al. (2021), we calculate the FPP and NFPP 20 times and report the mean value as the nominal value along with the 68% confidence interval.

5. Results

In this section, we present the results of our statistical analysis of each target individually, drawing on the high-

[38] https://github.com/JGB276/TRICERATOPS-plus.

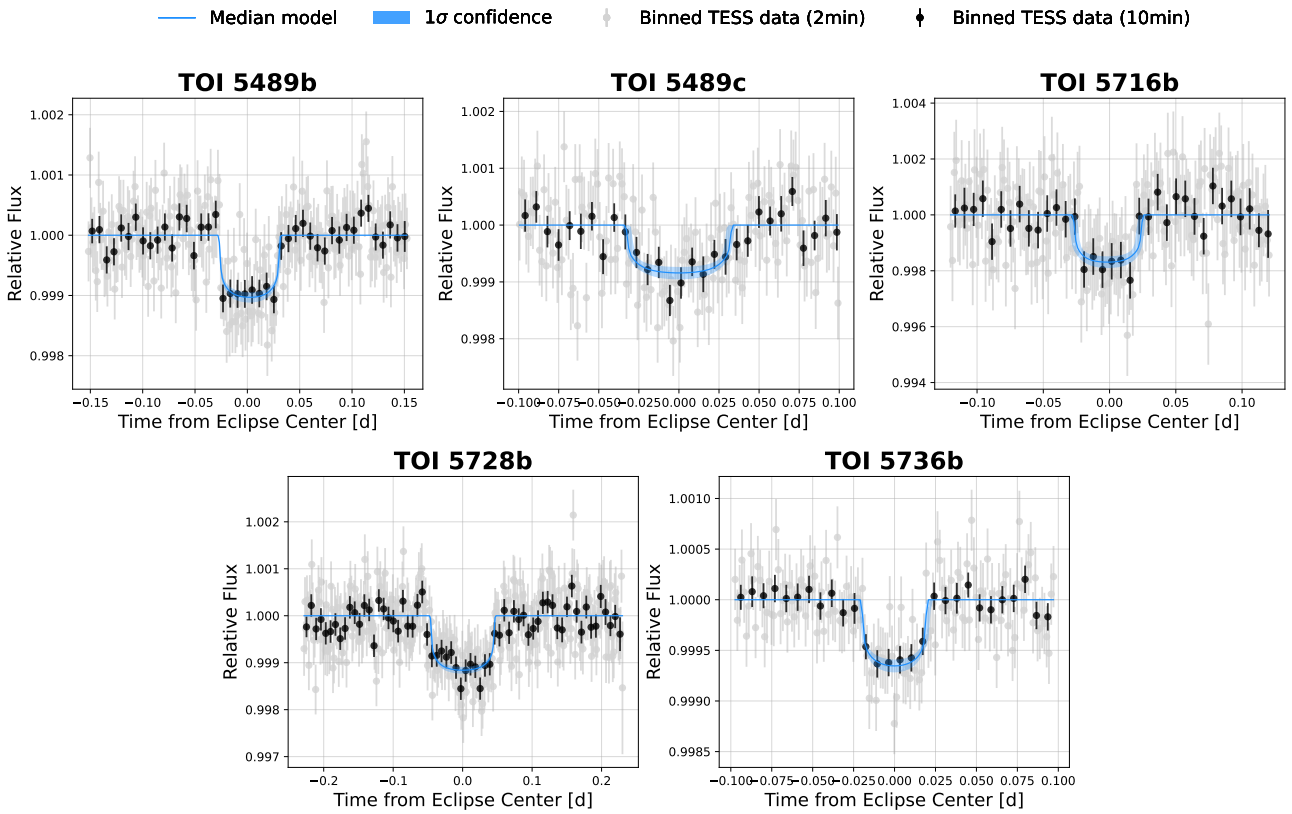


Figure 3. Stacked TESS light curves for our five targets. Gray points show the 2 minute binned data, and black points show the 10 minute binned data. The blue line represents the median transit model from the posterior distribution, with light blue shading indicating the 68% confidence interval.

resolution imaging, stellar spectroscopy, and multicolor transit photometry data presented earlier in this paper.

5.1. TOI-5489 b

TOI-5489.01 is a super-Earth-sized ($R_p = 1.40\ R_\oplus$) planet candidate that orbits its M dwarf host star ($V = 13.8$; $J = 10.3$) every 3.15 days. It was identified simultaneously by the QLP-FAINT and SPOC TPS pipelines (J. M. Jenkins 2002; J. M. Jenkins et al. 2010; C. X. Huang et al. 2020a, 2020b; J. M. Jenkins et al. 2020; M. Kunimoto & T. Daylan 2021). The QLP-FAINT pipeline employs a box least squares (G. Kovács et al. 2002) transit search algorithm while the SPOC transit search utilizes an adaptive, noise-compensating matched filter. Our observations indicate that TOI-5489.01 is a transiting planet. The high-resolution image from the PHARO instrument on Palomar in the K_{cont} filter shows no nearby stellar companions (see Figure 1). The phase-folded TESS light curve (Sectors 7–72) in Figure 3 shows a U-shaped transit signal, while the phase-folded LCOGT i-band light curve in Figure 4 indicates that the transit signal is slightly chromatic (inconsistent at the 1.2σ level). Our statistical validation analysis with TRICERATOPS+ finds that FPP $= 3 \times 10^{-4}$ (68% confidence interval of 2×10^{-4}–4×10^{-4}) and that the NFPP is zero, since there are no resolved stars inside the optimal aperture of the LCOGT light curve, based on the TESS photometry, LCOGT data, and the Palomar/PHARO contrast curve. With FPP < 0.015 and NFPP $< 10^{-3}$, TOI-5489.01 satisfies the criteria for a statistically validated planet and we hereafter refer to it as TOI-5489 b.

5.2. TOI-5489 c

TOI-5489.02 (also identified by the SPOC TPS pipeline; J. M. Jenkins 2002; J. M. Jenkins et al. 2010, 2020) is a super-Earth-sized ($R_p = 1.28\ R_\oplus$) planet candidate orbiting exterior to TOI-5489 b with a period of 4.92 days yielding a period ratio that places them within 4% of the 3:2 orbital resonance. While this proximity suggests potential dynamical interactions, Kepler systems near first-order resonance with significant long-term transit-timing variations typically show resonance proximity closer than 3% (see Table 8 of T. Holczer et al. 2016). Given this 4% separation, we adopt a linear ephemeris when stacking the TESS transits. Like TOI-5489.01, our observations indicate that TOI-5489.02 is also a transiting planet, consistent with previous studies demonstrating that candidates in multiplanet systems are much more likely to be bona fide planets (J. F. Rowe et al. 2014). The high-resolution image from Palomar/PHARO in the K_{cont} filter shows no nearby stellar companions (Figure 1). The phase-folded TESS light curve (Sectors 7–72; Figure 3) shows a U-shaped transit signal, while the phase-folded LCOGT i-band light curve and the Palomar J-band light curve indicate that the transit signal is achromatic (Figure 4). Our statistical validation analysis with TRICERATOPS+ incorporating the TESS photometry, LCOGT data, Palomar data, and the Palomar/PHARO contrast curve, indicates that FPP $= 3 \times 10^{-4}$ (68% confidence interval of 2×10^{-4}–4×10^{-4}) and that the NFPP is zero, as there are no resolved stars inside the optimal apertures of the ground-based light curves. We note that TRICERATOPS+ does not account for planet multiplicity when estimating the FPP of a given candidate (e.g., N. M. Guerrero et al. 2021) and thus the current estimate

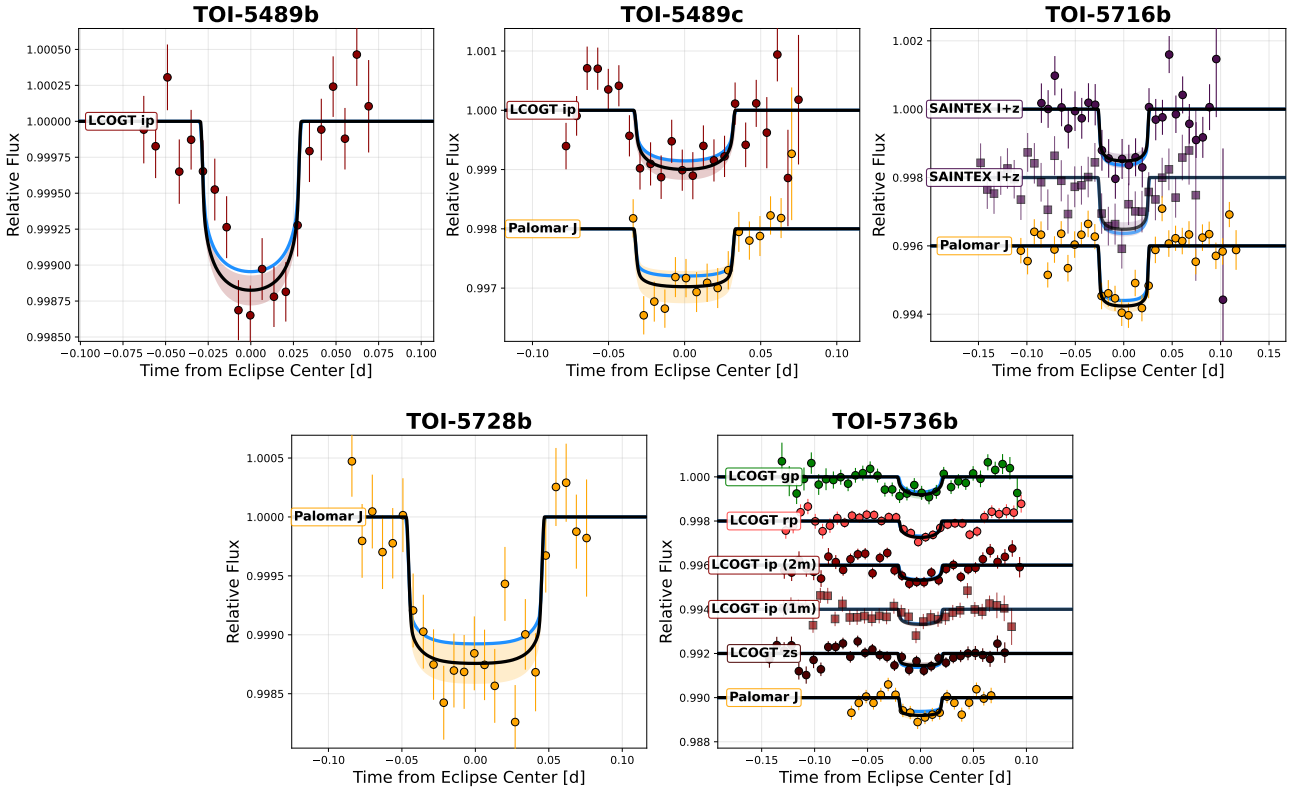


Figure 4. Multicolor ground-based light curves for our five targets. Data points represent 10 minute binned photometry, with light curves obtained using identical filters and exposure times phase folded together. Black curves show the median transit model derived from the posterior distribution, with colored shading indicating the 68% confidence intervals. Blue curves represent the nominal TESS light-curve model projected into the corresponding ground-based filters.

of this candidate is effectively an upper limit. Nevertheless, given these probabilities, TOI-5489.02 satisfies the criteria for a statistically validated planet and we hereafter refer to it as TOI-5489 c.

5.3. TOI-5716 b

TOI-5716.01 is an Earth-sized ($R_p = 0.96\ R_\oplus$) planet candidate orbiting a relatively faint M dwarf host star ($V = 15.8$; $J = 11.6$) every 6.77 days. It was first identified by the SPOC TPS pipeline (J. M. Jenkins 2002; J. M. Jenkins et al. 2010, 2020). Our observations indicate that TOI-5716.01 is a transiting planet. The high-resolution image from SAI-2.5 m (I. A. Strakhov et al. 2023) in the I filter shows no nearby stellar companions (Figure 1). The phase-folded TESS data (Sectors 14–75; Figure 3) show a U-shaped transit signal. Furthermore, the SAINT-EX $I + z$–filter data and the Palomar J-band data indicate that the transit signal is achromatic (Figure 4). Based on the TESS photometry, SAINT-EX data, Palomar data, and the SAI-2.5 m contrast curve, we find that FPP $= 4.3 \times 10^{-3}$ (68% confidence interval of 4.0×10^{-3}–4.6×10^{-3}). Since there are no resolved stars inside the optimal apertures of the ground-based light curves, the NFPP is zero. As a result, TOI-5716.01 satisfies the criteria for a statistically validated planet and we hereafter refer to it as TOI-5716 b.

5.4. TOI-5728 b

TOI-5728.01 (identified by the SPOC TPS pipeline; J. M. Jenkins 2002; J. M. Jenkins et al. 2010, 2020) is a super-Earth-sized ($R_p = 1.31\ R_\oplus$) planet candidate around a similarly faint M dwarf star ($V = 15.0$; $J = 11.0$). It orbits its host star every 11.50 days. Our observations indicate that TOI-5728.01 is a transiting planet. The high-resolution image from the NIRC2 instrument on Keck II in the K_{cont} filter shows no nearby stellar companions (Figure 1). The phase-folded TESS data (Sectors 14–86; Figure 3) show a U-shaped transit signal, while the Palomar J-band data confirm that the transit signal is achromatic (R_p/R_* from TESS and Palomar are consistent at 1σ; Figure 4). Based on the TESS photometry, Palomar data, and the Keck2/NIRC2 contrast curve, we find that FPP $= 2.3 \times 10^{-7}$ (68% confidence interval of 3.6×10^{-8}–1.5×10^{-6}) and that the NFPP is zero, since there are no resolved stars inside the optimal aperture of the Palomar light curve. Consequently, TOI-5728.01 satisfies the criteria for a statistically validated planet and we hereafter refer to it as TOI-5728 b.

5.5. TOI-5736 c

TOI-5736.01 (identified by the SPOC TPS pipeline; J. M. Jenkins 2002; J. M. Jenkins et al. 2010, 2020) is a super-Earth-sized ($R_p = 1.56\ R_\oplus$) planet candidate around an early M dwarf star ($V = 13.6$; $J = 10.8$). It orbits its host star every 0.65 days. Our observations indicate that TOI-5736.01 is a transiting planet. The high-resolution image from the NIRC2 instrument on Keck II in the K_{cont} filter shows no nearby stellar companions (Figure 1). The phase-folded TESS data (Sectors 16–77; Figure 3) show a U-shaped transit signal, while the LCOGT g, r, i, and z data and Palomar J-band data show that the transit signal is achromatic (Figure 4). With the TESS data, ground-based data, and the Keck2/NIRC2 contrast curve, we find that FPP $= 7 \times 10^{-5}$ (68% confidence interval of

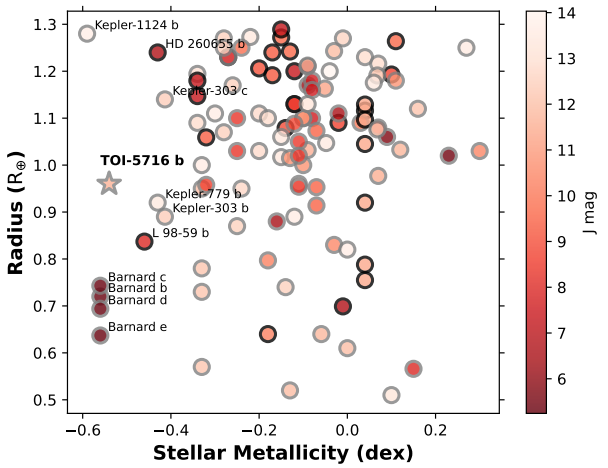


Figure 5. The population of small exoplanets around M dwarf stars ($T_* < 4000$ K) depicting the distribution of stellar metallicities for planet-hosting stars. Planets with published mass measurements $>3\sigma$ are highlighted in black whereas those without are highlighted in gray. The data points are colored based on their brightness in the J band as a guide for their accessibility to radial velocity measurements.

5×10^{-5}–9×10^{-5}). Given that there are no resolved stars inside the apertures of the ground-based light curves, we find that the NFPP is zero. Hence, TOI-5736.01 satisfies the criteria for a statistically validated planet and we hereafter refer to it as TOI-5736 b.

6. Discussion

Having validated the planetary nature of our targets, in this section we explore how they compare to the broader population of small planets around low-mass stars and discuss key properties.

6.1. Could TOI-5716 Be a Thick-disk Star?

To date, only a small number of confirmed exoplanets have been discovered orbiting thick-disk stars (e.g., T. L. Campante et al. 2015; T. Gan et al. 2020; L. M. Weiss et al. 2021; M. G. Scott et al. 2025). Despite the small size of this sample, comparative studies of planetary systems around stars from the thick versus thin disk have already begun to provide valuable insights into how stellar metallicity and age affect the formation and subsequent evolution of planetary systems. For instance, studies of exoplanets orbiting thick-disk stars have shown that Earth-sized planets have been forming throughout most of cosmic history, providing evidence for early planet formation in metal-poor environments (T. L. Campante et al. 2015). Furthermore, observations suggest that denser rocky planets are preferentially found around younger, more metal-rich stars (A. Weeks et al. 2025), though this claim has been disputed by subsequent analysis (A. Ross et al. 2025). Lastly, occurrence rate studies have found that there is a notable deficit in planets around thick-disk stars compared to the thin-disk population (D. Bashi & S. Zucker 2022; J. K. Zink et al. 2023; T. Hallatt & E. J. Lee 2025), suggesting that stellar metallicity and age play crucial roles in shaping planetary system architectures.

TOI-5716 has by far the lowest metallicity of all of the stars in our sample, and is only one of a handful of known planet-hosting stars with metallicities < -0.5 (see Figure 5). In light of this low metallicity, we investigated the possibility that this star might belong to the thick-disk population by applying the probabilistic framework developed by T. Bensby et al. (2014). Our analysis yielded a thick-disk to thin-disk probability ratio of 0.03, strongly favoring a thin-disk classification. As an additional check, we performed an orbital integration using the star's Gaia-derived proper motion and radial velocity measurements. We found that the star reaches a maximum vertical height of 1.2 kpc above the Galactic plane, which is higher than the 300–400 pc scale height of the Galactic thin disk. However, the eccentricity of the stellar orbit is low ($e = 0.046$), which is consistent with membership in the thin-disk population. Our detailed abundance analysis of the α-elements (O, Mg, and Ca) further supports the classification of the star as a thin-disk member. The star exhibits only mild α-enhancement, with a mean [α/Fe] ratio of $+0.07 \pm 0.08$ dex, consistent with enrichment from Type II and Type Ia supernovae, as expected for chemically evolved stars in the Galactic thin disk.

Although TOI-5716 belongs to the thin-disk population, its metal-poor composition still has important implications for the expected bulk composition of its Earth-sized transiting planet. Given the proposed correlation between planetary core mass fraction and host star metallicity for rocky exoplanets (V. Adibekyan et al. 2021; C. L. Brinkman et al. 2024), we anticipate that TOI-5716 b may have a lower core mass fraction than planets orbiting more metal-rich stars. This could be tested by obtaining a radial velocity mass measurement for this planet. To assess the feasibility of this measurement, we first calculated the expected radial velocity semiamplitude assuming an Earth-like bulk composition based on the mass–radius relationship from J. Chen & D. Kipping (2017), and found a predicted amplitude of 0.97 m s^{-1}. As shown in Figure 5, there are currently only two planets smaller than 1.3 $R_\oplus$ that have a published mass measurement orbiting an M dwarf star with a metallicity less than -0.4. HD 260655 b's mass was measured using radial velocities (R. Luque & E. Pallé 2022), but it orbits a much brighter host star ($J = 6.67$ versus 11.57 for TOI-5716) and has a larger radial velocity semiamplitude of 1.69 m s^{-1}. L 98-59 b's mass was also measured using radial velocities (R. Cloutier et al. 2019; O. D. S. Demangeon et al. 2021; C. Cadieux et al. 2025), and although it has a smaller radial velocity semiamplitude of 0.51 m s^{-1}, it also orbits a brighter star ($J = 7.93$ versus 11.57 for TOI-5716). We conclude that it will be challenging to measure TOI-5716 b's mass with current radial velocity instruments.

Studies have also indicated that metallicity can have a strong impact on the rotational evolution of low-mass stars (e.g., L. Amard & S. P. Matt 2020; V. See et al. 2024, 2025). For a fixed mass and age, metal-poor stars rotate faster than their solar-metallicity counterparts but have a higher stellar Rossby number, which is inversely proportional to stellar activity (L. Amard & S. P. Matt 2020). Therefore, TOI-5716 may exhibit lower stellar activity than more metal-rich stars, creating a more favorable stellar environment for TOI-5716 b and potentially enhancing the prospects for atmospheric retention.

6.2. Location of Newly Confirmed Super-Earth Planets Relative to the Cosmic Shoreline

Most M dwarf planets smaller than 1.5 $R_\oplus$ with measured masses appear to have densities consistent with Earth-like bulk

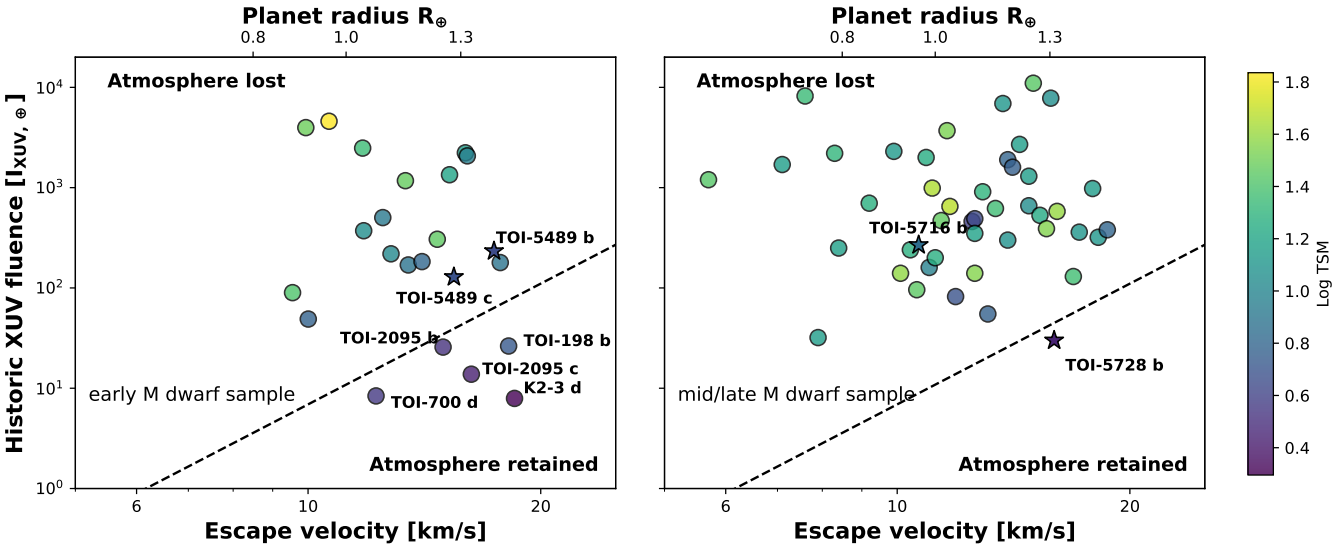


Figure 6. Left: the cosmic shoreline for early M dwarfs ($0.36\,M_{\odot} < M_{\star} < 0.6\,M_{\odot}$) from K. J. Zahnle & D. C. Catling (2017). Right: the cosmic shoreline for mid-to-late M dwarfs, as defined by E. K. Pass et al. (2025). In both panels the circles show the population of nearby (<50 pc) exoplanets with radii smaller than 1.5 $R_{\oplus}$ from the NASA Exoplanet Archive (accessed 2025 July 15; R. L. Akeson et al. 2013; NASA Exoplanet Archive 2024; J. L. Christiansen et al. 2025). Our targets are shown as stars. The colors of the data points correspond to their transmission spectroscopy metric (TSM). If confirmed to have an Earth-like bulk composition, TOI-5728 b would join the very small sample of rocky planets orbiting mid-to-late M dwarfs that are expected to have retained atmospheres.

compositions (R. Luque & E. Pallé 2022). If these planets have atmospheres they must be comprised of high mean molecular weight gases, and do not contribute significantly to the planet's measured radius. However, many close-in rocky planets orbiting M stars appear to have had their outgassed atmospheres stripped away by XUV irradiation, as discussed in Section 1. Here, we assess the likelihood that the planets in our sample with radii less than 1.5 $R_{\oplus}$ have retained high mean molecular weight atmospheres, and examine the feasibility of detecting atmospheric absorption features using transmission spectroscopy.

In Figure 6, we show the population of nearby M dwarf exoplanets (<50 pc) smaller than 1.5 $R_{\oplus}$ as a function of historic XUV fluence and escape velocity. We plot the sample of planets orbiting early M dwarfs and mid-to-late M dwarfs separately, and calculate the XUV fluence and cosmic shoreline location following K. J. Zahnle & D. C. Catling (2017) for the early M dwarf sample and E. K. Pass et al. (2025) for the mid-to-late M dwarf sample. For planets without a mass measurement, including the four new planets reported here, we assume an Earth-like bulk density and adopt the mass–radius relationship presented in J. Chen & D. Kipping (2017) to calculate their escape velocities. As shown in Figure 6, TOI-5489 b and TOI-5489 c lie above the predicted cosmic shoreline and therefore may have lost their atmospheres; however, their proximity to the shoreline means that observational limits on their atmospheric masses would help to constrain the location and slope of this boundary. For mid-to-late M dwarfs, Figure 6 shows that almost all currently known targets lie above the cosmic shoreline, including TOI-5716 b. However, TOI-5728 b lies below the shoreline, suggesting that it is more likely to have retained its atmosphere. This is consistent with findings from E. K. Pass et al. (2025), who note that only the largest terrestrial planets around mid-to-late M dwarfs are expected to retain their atmospheres. TOI-5728 b has a predicted radial velocity semiamplitude of 1.5 m s^{-1} and orbits an optically faint star ($V = 15.83$; $J = 11.57$), suggesting that it will be challenging to confirm whether or not this planet has an Earth-like bulk density via a radial velocity mass measurement.

Next, we explore the detectability of atmospheric absorption features during the transit using the TSM (E. M. R. Kempton et al. 2018). As shown in Figure 6, the four planets in our sample have TSM values below the typical threshold value of 12 for planets with $R_p < 1.5\,R_{\oplus}$, which is generally considered to be a lower bound for atmospheric characterization studies with JWST (E. M. R. Kempton et al. 2018). Although this suggests that it would require a significant investment of telescope time to obtain a useful transmission spectrum, this may be justified by TOI-5728 b's unique position as the only validated planet that lies below the cosmic shoreline for mid-to-late M dwarfs.

6.3. Does TOI-5736 b Have a Volatile-rich Envelope?

TOI-5736 b has the highest equilibrium temperature (1311 K) and largest radius ($1.56 \pm 0.07\,R_{\oplus}$) of the planets in our sample. If we compare TOI-5736 b to the sample of M dwarf planets with measured masses and radii (e.g., R. Luque & E. Pallé 2022; F. Wanderley et al. 2025), we find that it is on the upper end of the range for planets with Earth-like bulk compositions. Alternatively, it could have retained a volatile-rich envelope despite its relatively high XUV irradiation level. TOI-1634 b (e.g., R. Cloutier et al. 2021) is similar in size and also orbits an M dwarf on a subday orbital period (see Figure 7). Radial velocity observations of this planet indicate that it has retained a volatile-rich atmosphere, but it also receives a bolometric flux that is approximately a factor of 3 less than that of TOI-5736 b.

If the mass of TOI-5736 b could be measured using the radial velocity technique, it would be straightforward to determine whether or not it also hosts a volatile-rich envelope. Assuming an Earth-like bulk density based on the mass–radius relationship presented in J. Chen & D. Kipping (2017), TOI-5736 b is expected to have a radial velocity semiamplitude of 5.5 m s^{-1}. This is comparable to the measured radial velocity semiamplitude of TOI-1634 b (5.1 ± 0.8 m s^{-1}; R. Cloutier et al. 2021)

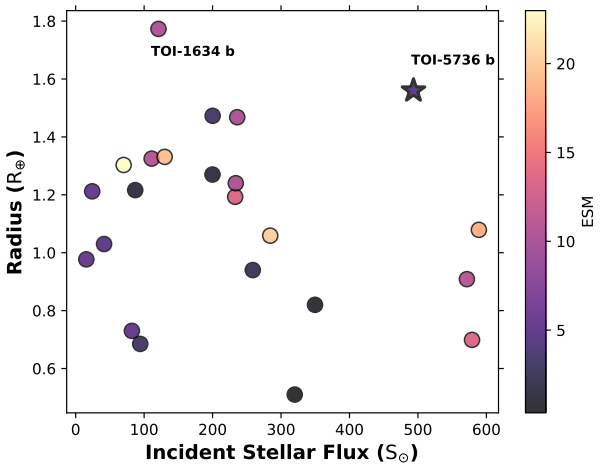


Figure 7. The population of ultrashort-period ($P < 1$ day) planets smaller than 1.8 $R_\oplus$ around M stars. The planets are colored based on their emission spectroscopy metric (ESM). TOI-5736 b has a predicted equilibrium temperature of 1311 K and an ESM of four.

and the two stars are similarly bright ($V = 13.55$ and $J = 10.83$ for TOI-5736; $V = 13.22$ and $J = 9.48$ for TOI-1634). This suggests that it should be straightforward to measure TOI-5736 b's mass with current radial velocity instruments. Alternatively, the presence or absence of a thick atmosphere can also be constrained by measuring thermal emission from the planet's dayside. We quantify the relative favorability of TOI-5736 b for this measurement using the ESM (E. M. R. Kempton et al. 2018), as indicated by the colored shading in Figure 7.

7. Conclusions

In this paper, we statistically validate five small transiting planets around M dwarfs using 2 minute TESS light curves, multicolor ground-based light curves, and high-resolution imaging. The sample consists of TOI-5489 b, TOI-5489 c, TOI-5716 b, TOI-5728 b, and TOI-5736 b. These five planets span a range of orbital periods, from TOI-5736 b, which orbits its host every 15.6 hours, to TOI-5728 b, which has an orbital period of 11.50 days. Although the targets in this sample will be challenging for atmospheric studies compared to other similar systems, these systems represent an important addition to the sample of planets that could be used to test the cosmic shoreline framework. If radial velocity measurements confirm an Earth-like density, TOI-5728 b would join the population of small planets around mid-to-late M stars that lie below the cosmic shoreline.

Acknowledgments

We thank the anonymous referee for a helpful report. We would like to thank the Palomar Observatory staff and telescope operators, including Kathleen Koviak, Paul Nied, Diana Roderick, Rigel Rafto, and John Stone for their assistance with the observations of TOI-5489, TOI-5716, TOI-5728, and TOI-5736. This work is based on observations obtained at the Hale Telescope, Palomar Observatory, as part of a collaborative agreement between the Caltech Optical Observatories and the Jet Propulsion Laboratory (operated by Caltech for NASA). Some of the observations presented in this paper were carried out at the Observatorio Astronómico Nacional on the Sierra de San Pedro Mártir (OAN-SPM), Baja California, México.

This research was carried out at the Jet Propulsion Laboratory and the California Institute of Technology under a contract with the National Aeronautics and Space Administration and funded through the President's and Director's Research and Development Fund Program. We also acknowledge support from the Swiss National Science Foundation SPIRIT-216537 and the Centre for Space and Habitability (CSH) of the University of Bern. Part of this work received support from the National Centre for Competence in Research Planets, supported by the Swiss National Science Foundation (SNSF). Y.G.M.C. and A.K. are partially supported by UNAM PAPIIT-IG101224. B.-O.D. acknowledges support from the Swiss State Secretariat for Education, Research and Innovation (SERI) under contract No. MB22.00046.

This paper includes data collected by the TESS mission that are publicly available from the Mikulski Archive for Space Telescopes (MAST). The specific observations analyzed can be accessed via DOI: 10.17909/c3pd-m382. Funding for the TESS mission is provided by NASA's Science Mission Directorate. We acknowledge the use of public TESS data from pipelines at the TESS Science Office and at the TESS Science Processing Operations Center. Resources supporting this work were provided by the NASA High-End Computing (HEC) Program through the NASA Advanced Supercomputing (NAS) Division at Ames Research Center for the production of the SPOC data products. This research has made use of the Exoplanet Follow-up Observation Program website, which is operated by the California Institute of Technology, under contract with the National Aeronautics and Space Administration under the Exoplanet Exploration Program.

We acknowledge financial support from the Agencia Estatal de Investigación of the Ministerio de Ciencia e Innovación MCIN/AEI/10.13039/501100011033 and the ERDF "A way of making Europe" through project PID2021-125627OB-C32, and from the Centre of Excellence "Severo Ochoa" award to the Instituto de Astrofisica de Canarias.

This work makes use of observations from the Las Cumbres Observatory global telescope network.

This material is based upon work supported by the National Science Foundation Graduate Research Fellowship Program under grant No. DGE-1745301.

M.G. is FNRS Research Director.

F.M. acknowledges the financial support from the Agencia Estatal de Investigación del Ministerio de Ciencia, Innovación y Universidades (MCIU/AEI) through grant PID2023-152906NA-I00.

W.G.L. gratefully acknowledges support from the Department of Defense's National Defense Science and Engineering Graduate (NDSEG) Fellowship. W.G.L. also thanks the LSST-DA Data Science Fellowship Program, which is funded by LSST-DA, the Brinson Foundation, the WoodNext Foundation, and the Research Corporation for Science Advancement Foundation; his participation in the program has benefited this work.

M.L. acknowledges support of the Swiss National Science Foundation under grant no. PCEFP2194576. The contribution of M.L. has been carried out within the framework of the NCCR Planets supported by the Swiss National Science Foundation under grant 51NF40205606.

This work is partly supported by JSPS KAKENHI grant No. JP24H00017 and JSPS Bilateral Program No. JPJSBP120249910. This paper is based on observations made with the MuSCAT

instruments, developed by the Astrobiology Center (ABC) in Japan, the University of Tokyo, and Las Cumbres Observatory (LCOGT). MuSCAT3 was developed with financial support by JSPS KAKENHI (JP18H05439) and JST PRESTO (JPMJPR1775), and is located at the Faulkes Telescope North on Maui, HI (USA), operated by LCOGT.

Y.G.M.C. and B.-O. D. acknowledge support from the Swiss National Science Foundation (IZSTZ0216537).

D.S. acknowledges support from the Foundation for Research and Technological Innovation Support of the State of Sergipe (FAPITEC/SE) and the National Council for Scientific and Technological Development (CNPq), under grant Nos. 794017/2013 and 444372/2024-5.

D.R.C. acknowledges partial support from NASA grant 182XRP182-0007.

Some of the data presented herein were obtained at Keck Observatory, which is a private 501(c)3 nonprofit organization operated as a scientific partnership among the California Institute of Technology, the University of California, and the National Aeronautics and Space Administration. The Observatory was made possible by the generous financial support of the W. M. Keck Foundation.

The authors wish to recognize and acknowledge the very significant cultural role and reverence that the summit of Maunakea has always had within the Native Hawaiian community. We are most fortunate to have the opportunity to conduct observations from this mountain.

ORCID iDs

Jonathan Gomez Barrientos https://orcid.org/0000-0002-0672-9658
Heather A. Knutson https://orcid.org/0000-0002-5375-4725
Morgan Saidel https://orcid.org/0000-0001-9518-9691
Michael Greklek-McKeon https://orcid.org/0000-0002-0371-1647
W. Garrett Levine https://orcid.org/0000-0002-1422-4430
Nicholas Saunders https://orcid.org/0000-0003-2657-3889
Howard Isaacson https://orcid.org/0000-0002-0531-1073
Renyu Hu https://orcid.org/0000-0003-2215-8485
Karen A. Collins https://orcid.org/0000-0001-6588-9574
David R. Ciardi https://orcid.org/0000-0002-5741-3047
Polina A. Budnikova https://orcid.org/0009-0002-0733-572X
Dmitry V. Cheryasov https://orcid.org/0009-0003-4203-9667
Samuel W. Yee https://orcid.org/0000-0001-7961-3907
Diogo Souto https://orcid.org/0000-0002-7883-5425
Aida Behmard https://orcid.org/0000-0003-0012-9093
Akihiko Fukui https://orcid.org/0000-0002-4909-5763
Avi Shporer https://orcid.org/0000-0002-1836-3120
Akanksha Khandelwal https://orcid.org/0000-0003-0335-6435
Bob Massey https://orcid.org/0000-0001-8879-7138
Brice-Oliver Demory https://orcid.org/0000-0002-9355-5165
Catherine A. Clark https://orcid.org/0000-0002-2361-5812
Chris Stockdale https://orcid.org/0000-0003-2163-1437
Emily A. Gilbert https://orcid.org/0000-0002-0388-8004
Enric Palle https://orcid.org/0000-0003-0987-1593
Francis P. Wilkin https://orcid.org/0000-0003-2127-8952
Felipe Murgas https://orcid.org/0000-0001-9087-1245
Jessie L. Christiansen https://orcid.org/0000-0002-8035-4778
Jon M. Jenkins https://orcid.org/0000-0002-4715-9460
Joseph D. Twicken https://orcid.org/0000-0002-6778-7552
Keith Horne https://orcid.org/0000-0003-1728-0304
Michaël Gillon https://orcid.org/0000-0003-1462-7739
Monika Lendl https://orcid.org/0000-0001-9699-1459
Michael B. Lund https://orcid.org/0000-0003-2527-1598
Norio Narita https://orcid.org/0000-0001-8511-2981
Pam Rowden https://orcid.org/0000-0002-4829-7101
Ramotholo Sefako https://orcid.org/0000-0003-3904-6754
Richard P. Schwarz https://orcid.org/0000-0001-8227-1020
Steven Giacalone https://orcid.org/0000-0002-8965-3969
Urs Schroffenegger https://orcid.org/0009-0005-5046-203X
Yilen Gómez Maqueo Chew https://orcid.org/0000-0002-7486-6726

References

Adibekyan, V., Dorn, C., Sousa, S. G., et al. 2021, Sci, 374, 330
Ahumada, R., Allende Prieto, C., Almeida, A., et al. 2020, ApJS, 249, 3
Akeson, R. L., Chen, X., Ciardi, D., et al. 2013, PASP, 125, 989
Allard, F., Hauschildt, P. H., Alexander, D. R., Tamanai, A., & Schweitzer, A. 2000, ApJ, 540, 1005
Amard, L., & Matt, S. P. 2020, ApJ, 889, 108
Bashi, D., & Zucker, S. 2022, MNRAS, 510, 3449
Bensby, T., Feltzing, S., & Oey, M. S. 2014, A&A, 562, A71
Berger, T. A., Huber, D., van Saders, J. L., et al. 2020, AJ, 159, 280
Berger, T. A., Schlieder, J. E., & Huber, D. 2023, arXiv:2301.11338
Birky, J., Hogg, D. W., Mann, A. W., & Burgasser, A. 2020, ApJ, 892, 31
Brinkman, C. L., Polanski, A. S., Huber, D., et al. 2024, AJ, 168, 281
Brown, T. M., Baliber, N., Bianco, F. B., et al. 2013, PASP, 125, 1031
Cadieux, C., L'Heureux, A., Piaulet-Ghorayeb, C., et al. 2025, AJ, 170, 154
Campante, T. L., Barclay, T., Swift, J. J., et al. 2015, ApJ, 799, 170
Casey, A. R., Hogg, D. W., Ness, M., et al. 2016, arXiv:1603.03040
Chen, J., & Kipping, D. 2017, ApJ, 834, 17
Choi, J., Dotter, A., Conroy, C., et al. 2016, ApJ, 823, 102
Christiansen, J. L., McElroy, D. L., Harbut, M., et al. 2025, PSJ, 6, 186
Cloutier, R., Astudillo-Defru, N., Bonfils, X., et al. 2019, A&A, 629, A111
Cloutier, R., Charbonneau, D., Stassun, K. G., et al. 2021, AJ, 162, 79
Collaboration, S., Pallathadka, G. A., Aghakhanloo, M., et al. 2025, arXiv:2507.07093
Collins, K. A., Kielkopf, J. F., Stassun, K. G., & Hessman, F. V. 2017, AJ, 153, 77
Dekany, R., Roberts, J., Burruss, R., et al. 2013, ApJ, 776, 130
Demangeon, O. D. S., Zapatero Osorio, M. R., Alibert, Y., et al. 2021, A&A, 653, A41
Demory, B. O., Pozuelos, F. J., Gómez Maqueo Chew, Y., et al. 2020, A&A, 642, A49
Fleming, D. P., Barnes, R., Luger, R., & VanderPlas, J. T. 2020, ApJ, 891, 155
Fortune, M., Gibson, N. P., Diamond-Lowe, H., et al. 2025, A&A, 701, A25
Furlan, E., Ciardi, D. R., Everett, M. E., et al. 2017, AJ, 153, 71
Gan, T., Shporer, A., Livingston, J. H., et al. 2020, AJ, 159, 160
Giacalone, S., Dressing, C. D., Jensen, E. L. N., et al. 2021, AJ, 161, 24
Gomez Barrientos, J., Greklek-McKeon, M., Knutson, H. A., et al. 2025, AJ, 170, 148
Gómez Maqueo Chew, Y., Demory, B. O., Sabin, L., et al. 2023, RMxAC, 55, 46
Grant, D., & Wakeford, H. R. 2022, Exo-TiC/ExoTiC-LD: ExoTiC-LD, v3.0.0, Zenodo, doi:10.5281/zenodo.7437681
Greene, T. P., Bell, T. J., Ducrot, E., et al. 2023, Natur, 618, 39
Greklek-McKeon, M., Knutson, H. A., Vissapragada, S., et al. 2023, AJ, 165, 48
Guerrero, N. M., Seager, S., Huang, C. X., et al. 2021, ApJS, 254, 39
Hallatt, T., & Lee, E. J. 2025, ApJ, 979, 120
Hayward, T. L., Brandl, B., Pirger, B., et al. 2001, PASP, 113, 105
Henry, T. J., Kirkpatrick, J. D., & Simons, D. A. 1994, AJ, 108, 1437
Hoffman, M. D., & Gelman, A. 2011, arXiv:1111.4246
Holczer, T., Mazeh, T., Nachmani, G., et al. 2016, ApJS, 225, 9
Hori, Y., & Ogihara, M. 2020, ApJ, 889, 77
Huang, C. X., Vanderburg, A., Pál, A., et al. 2020a, RNAAS, 4, 204
Huang, C. X., Vanderburg, A., Pál, A., et al. 2020b, RNAAS, 4, 206
Huber, D., Zinn, J., Bojsen-Hansen, M., et al. 2017, ApJ, 844, 102
Jenkins, J. M. 2002, ApJ, 575, 493
Jenkins, J. M., Chandrasekaran, H., McCauliff, S. D., et al. 2010, SPIE, 7740, 77400D
Jenkins, J. M., Twicken, J. D., McCauliff, S., et al. 2016, SPIE, 9913, 99133E
Jenkins, J. M., Tenenbaum, P., Seader, S., et al. 2020, Kepler Data Processing Handbook: Transiting Planet Search KSCI-19081-003, Kepler
Katz, D., Sartoretti, P., Guerrier, A., et al. 2023, A&A, 674, A5

Kempton, E. M. R., Bean, J. L., Louie, D. R., et al. 2018, PASP, 130, 114401
Kipping, D. M. 2013, MNRAS, 434, L51
Kirkpatrick, J. D., Reid, I. N., Liebert, J., et al. 1999, ApJ, 519, 802
Kollmeier, J. A., Rix, H.-W., Aerts, C., et al. 2026, AJ, 171, 52
Kovács, G., Zucker, S., & Mazeh, T. 2002, A&A, 391, 369
Kreidberg, L., & Stevenson, K. B. 2025, PNAS, 122, e2416190122
Kunimoto, M., & Daylan, T. 2021, Searching for Exoplanets Around Faint Stars in TESS FFIs, v1, Zenodo, doi:10.5281/zenodo.5125527
Lightkurve Collaboration, Cardoso, J. V. d. M., Hedges, C., et al., 2018 Lightkurve: Kepler and TESS Time Series Analysis in Python,Astrophysics Source Code Library, ascl:1812.013
Lomb, N. R. 1976, Ap&SS, 39, 447
Luger, R., Agol, E., Foreman-Mackey, D., et al. 2019, AJ, 157, 64
Luque, R., & Pallé, E. 2022, Sci, 377, 1211
Luque, R., Coy, B. P., Xue, Q., et al. 2025, AJ, 170, 49
Mann, A. W., Feiden, G. A., Gaidos, E., Boyajian, T., & von Braun, K. 2015, ApJ, 804, 64
Mann, A. W., Dupuy, T., Kraus, A. L., et al. 2019, ApJ, 871, 63
McCully, C., Volgenau, N. H., Harbeck, D.-R., et al. 2018, SPIE, 10707, 107070K
Meier Valdés, E. A., Demory, B. O., Diamond-Lowe, H., et al. 2025, A&A, 698, A68
Melo, E., Souto, D., Cunha, K., et al. 2024, ApJ, 973, 90
Narita, N., Fukui, A., Yamamuro, T., et al. 2020, SPIE, 11447, 114475K
NASA Exoplanet Archive 2024, Stellar Parameters for Planetary Hosts Table, NASA IPAC, doi:10.26133/NEA12
Ness, M., Hogg, D. W., Rix, H. W., Ho, A. Y. Q., & Zasowski, G. 2015, ApJ, 808, 16
Nidever, D. L., Holtzman, J. A., Prieto, C. A., et al. 2015, AJ, 150, 173
Nutzman, P., & Charbonneau, D. 2008, PASP, 120, 317
Pass, E. K., Charbonneau, D., & Vanderburg, A. 2025, ApJL, 986, L3
Roettenbacher, R. M., & Kane, S. R. 2017, ApJ, 851, 77
Ross, A., Reggiani, H., Schlaufman, K. C., Plotnykov, M., & Valencia, D. 2025, ApJ, 993, 235
Rowe, J. F., Bryson, S. T., Marcy, G. W., et al. 2014, ApJ, 784, 45
Scargle, J. D. 1982, ApJ, 263, 835
Schwarz, G. 1978, AnSta, 6, 461
Scott, M. G., Triaud, A. H. M. J., Barkaoui, K., et al. 2025, MNRAS, 540, 1909
See, V., Lu, Y. L., Amard, L., & Roquette, J. 2024, MNRAS, 533, 1290
See, V., Fairman, C., Amard, L., & Hall, O. 2025, MNRAS, 544, 1649
Smith, J. C., Stumpe, M. C., Van Cleve, J. E., et al. 2012, PASP, 124, 1000
Souto, D., Cunha, K., Smith, V. V., et al. 2020, ApJ, 890, 133
Souto, D., Cunha, K., & Smith, V. V. 2021, ApJ, 917, 11
Stassun, K. G., Oelkers, R. J., Paegert, M., et al. 2019, AJ, 158, 138
Stefansson, G., Mahadevan, S., Hebb, L., et al. 2017, ApJ, 848, 9
Stetson, P. B. 1987, PASP, 99, 191
Strakhov, I. A., Safonov, B. S., & Cheryasov, D. V. 2023, AstBu, 78, 234
Stumpe, M. C., Smith, J. C., Van Cleve, J. E., et al. 2012, PASP, 124, 985
Stumpe, M. C., Smith, J. C., Catanzarite, J. H., et al. 2014, PASP, 126, 100
Vissapragada, S., Jontof-Hutter, D., Shporer, A., et al. 2020, AJ, 159, 108
Vogt, S. S., Allen, S. L., Bigelow, B. C., et al. 1994, SPIE, 2198, 362
Wachiraphan, P., Berta-Thompson, Z. K., Diamond-Lowe, H., et al. 2025, AJ, 169, 311
Wanderley, F., Cunha, K., Smith, V. V., et al. 2025, ApJ, 993, 233
Weeks, A., Van Eylen, V., Huber, D., et al. 2025, MNRAS, 539, 405
Weiss, L. M., Dai, F., Huber, D., et al. 2021, AJ, 161, 56
Wilson, J. C., Eikenberry, S. S., Henderson, C. P., et al. 2003, SPIE, 4841, 451
Wilson, R. F., Teske, J., Majewski, S. R., et al. 2018, AJ, 155, 68
Wizinowich, P., Acton, D. S., Shelton, C., et al. 2000, PASP, 112, 315
Wordsworth, R., & Kreidberg, L. 2022, ARA&A, 60, 159
Xue, Q., Bean, J. L., Zhang, M., et al. 2024, ApJL, 973, L8
Yee, S. W., Petigura, E. A., & von Braun, K. 2017, ApJ, 836, 77
Zahnle, K. J., & Catling, D. C. 2017, ApJ, 843, 122
Zhang, M., Hu, R., Inglis, J., et al. 2024, ApJL, 961, L44
Zieba, S., Kreidberg, L., Ducrot, E., et al. 2023, Natur, 620, 746
Zink, J. K., Hardegree-Ullman, K. K., Christiansen, J. L., et al. 2023, AJ, 165, 262